Hindawi

Research Article

Data Mining-Based Design Space Exploration and Optimization for Tandem Airfoils

Yayun Shi [ID],[1] **Xiayu Lan** [ID],[2] **Yiwen Wang** [ID],[2] **Tihao Yang** [ID],[2] **and Yan Liu** [ID][3]

[1]*Xi'an Jiaotong University, Xi'an, Shaanxi 710049, China*
[2]*Northwestern Polytechnical University, Xi'an, Shaanxi 710072, China*
[3]*Shenyang Aircraft Design Institute, Shenyang, Liaoning 110036, China*

Correspondence should be addressed to Tihao Yang; yangtihao@nwpu.edu.cn

The joined-wing configuration has great technical appeal for the development of next-generation SensorCraft. Research based on the simplified tandem airfoil system can improve understanding of the joined-wing configuration's aerodynamic characteristics. We combine the adjoint-based aerodynamic shape optimization and self-organizing map- (SOM-) based data mining technology to reveal the flow interactions of tandem airfoils and aerodynamic characteristics from the perspective of the entire aerodynamic design space. The SOM is used to explore the correlation between relative position parameters and aerodynamic force coefficients of tandem airfoil systems. Results show that the drag coefficient at the defined range of lift coefficients has obviously positive linear correlation and greatly dependents on the value of decalage. The tandem airfoils with negative decalage around -2.7° have the smallest drag coefficients. Due to variations in the aerodynamic interaction strength, the drag coefficient of each airfoil changes from a linear law to a nonlinear law as airfoils approach each other. We then perform single-point aerodynamic shape optimization based on two sets of relative position parameters with different aerodynamic interaction strengths, and 1.8% and 1.28% drag reductions are obtained, respectively. Based on optimized airfoils, the SOM is used to reveal the distribution of drag variation in the design space constructed by relative position parameters. Results illustrate that the aerodynamic interference strength between the front and rear airfoils significantly affects the drag reduction mechanism, which results in the different distribution patterns of drag variation in design space.

1. Introduction

The SensorCraft concept was initiated by the Air Force Research Lab (AFRL) to inspire innovation and cutting-edge technology. The driving design objective is the integration of the sensing functionality into a high-altitude long-endurance (HALE) unmanned aerial vehicle, which has the capacity of a full 360° radar coverage and more than 30 hr of endurance [1]. These technical requirements significantly increase the design difficulty of unmanned aerial vehicles (UAVs). Therefore, new configurations and novel technology are needed. Compared to other potential configurations, the joined-wing aircraft is considered exceedingly attractive for SensorCraft [2].

Joined wing presents a structure with two wings having approximately the same span. Generally, the front wing is the main one and is located in a lower position than the rear wing. The two wings are connected at their tips through a vertical element or direct connection at the outer part of the main wing. The layout characteristics of the joined wing allow a full 360° coverage with sensors integrated into the wing panels. Besides, it owns considerable locations for aerodynamic control surfaces on both the front and rear wings. Another advantage is the potential reduction of wing structure weight and induced drag concerning wing-body-tail configuration [2–4]. Due to its larger solar array area, the joined-wing aircraft is a valid alternative for solar-powered HALE vehicles [5–7]. Italian Aerospace Research Program

(CIRA) has studied a joined-wing concept of a solar-powered HALE UAV with an 80 m span, which can fly 20 days at a cruise velocity of 33.3 m/s [8].

The layout characteristic of joined wing presents a unique flow physics phenomenon. Compared to the traditional monoplane configuration, the joined wing has apparent and complex aerodynamic coupling interference between the front and rear wings. The flow around each wing is significantly affected by the other wing. The presence of each wing causes the other wing to be immersed in a distorted flow. Thus, the design of joined wings must consider the induced flow. The joined region plays the main role in those aerodynamic coupling phenomena. However, away from the joined region, this aerodynamic coupling effect degrades gradually as the spacing between the front and rear wings increases. The system can be simplified as a two-dimensional tandem airfoil with similar coupling effects. Except for the shape of airfoils, the aerodynamic interference heavily depends on the relative position. Smith [9] referred to the aerodynamic coupling in terms of five effects, including the slat effect, circulation effect, dumping effect, off-the-surface pressure recovery, and fresh boundary-layer effect.In general, the tandem airfoils [10] are used to research the flow mechanism and reveal the influence law of aerodynamic interference. Three main relative position parameters, namely, stagger, gap, and decalage (details of those parameters will be prescribed in Section 4.2, see in Figure 1), affect the aerodynamic performance of the tandem airfoil with the same airfoils and equal chords. The stagger defines the longitudinal separation of the wings. The gap describes the vertical distance between the wings. Both stagger and gap are nondimensionalized by the chord of airfoils. The decalage is the relative angle between the two airfoils.

Rokhsaz [11] studied the aerodynamic performance of tandem airfoils based on the NACA 63_2-215 airfoil. The result indicated that the most favorable configuration has a stagger of 1.0, a gap of 0.26, and a decalage of -6°. Rhodes and Selberg [12] carried out detailed parametric research to determine the aerodynamic influence relationship of stagger, gap, and decalage. They found that the positive-stagger and negative-decalage configurations performed well. Wolkovitch [1] discussed the effect of airfoil camber and found that a small airfoil camber of the rear wing benefits drag reduction. LeDoux et al. [13] have done similar work, and the optimization supported the conclusions of Wolkovitch. Moschetta and Thipyopas [14] performed wind tunnel tests to investigate the aerodynamic performance of tandem wings at a low Reynolds number. They revealed that the lift coefficient was strongly affected by the gap but not so much by the stagger. Jones et al. [15] also performed wind tunnel tests and found optimal gaps for improving the lift coefficient at a fixed angle of attack.

It is quite clear that the aerodynamic performance of tandem airfoils is dependent on the shape of the airfoils and their relative position. Many studies have been implemented to discuss aerodynamic interference and draw valuable conclusions. However, most of these works focus on parameter study within a limited range of variation or shape optimization with fixed relative positions. A comprehensive consideration is required for a complex engineering system
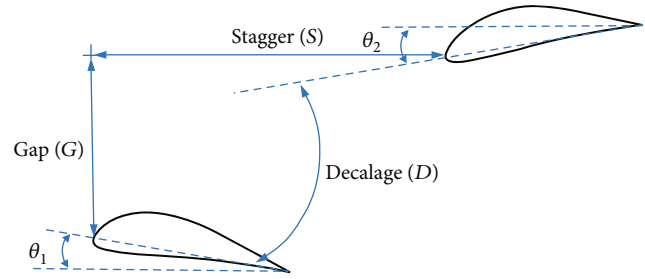

FIGURE 1: The definition of tandem airfoil relative position parameters.

in aircraft design. For joined-wing aircraft, the difference in aircraft size and performance requirement results in significant variations in layout parameters. Until now, deep insights into the design space characteristics of tandem airfoils remain unexplored. The coupling influence of relative positions and the airfoil shape in detail is also significant and required. In conclusion, there remain many works in understanding the flow physics and the effect of flow interference of tandem airfoils from the perspective of the entire aerodynamic design space.

A full understanding of an optimization problem's design space is the key to obtaining the best compromise design for all objective functions. The emergence of data mining [16] and deep learning [17] provides promising technologies to help explore the whole design space [18], guide the optimization, and understand the optimization result. Data mining is the process of analyzing data and transforming it into useful information [19–21]. Due to the complexity of optimization problems, it is difficult for designers to understand the inherent trade-offs and relations between design variables and objectives. Data mining can provide insight into the design of complex systems.

Researchers have introduced data mining into aerodynamic optimization design. Chiba and Obayashi [22] used three data mining techniques to successfully analyze the result of aerodynamic design optimization of a two-stage-to-orbit reusable launch vehicle flyback-booster wing. Oyama et al. [23] used the data mining method based on proper orthogonal decomposition to extract design information from the Pareto optimal solutions of aerodynamic shape optimization about airfoils. For the optimization design of a high-pressure ratio centrifugal impeller, Guo et al. [24] utilized a self-organizing map (SOM-) based data mining on the Pareto optimal solutions to analyze the interactions among objective functions and significant design variables. By now, research about the application of data mining in aerodynamic design optimization is still limited. Besides, most of the research focuses on the analysis of the Pareto optimal solutions [25], not understanding the whole design space.

According to the above content, this paper contributes to understanding the tandem airfoil aerodynamic interferences and design space characteristics, aiming to improve the performance of low-speed joined-wing UAVs. A high-fidelity CFD-based aerodynamic optimization framework with the adjoint-based approach [26] is used for tandem airfoil

optimizations, and the SOM-based [27] data mining method is utilized to explore the whole aerodynamic design space and reveal the influence law of aerodynamic interference.

The paper is organized as follows. Firstly, a brief overview of the adopted CFD solver and adjoint-based optimization frame is presented in Section 2. The basic theory of SOM is subsequently introduced in Section 3. Then, optimization design problems are defined, and SOM-based design space exploration with relative position parameters as design variables is discussed to understand correlations among design variables and aerodynamic performance in the whole design space (Section 4). After this, aerodynamic shape optimizations with the fixed relative positions are discussed to reveal the effect of airfoil shapes on aerodynamic forces in the whole design space (Section 5). Finally, we summarize our work.

2. CFD Solution and Optimization Methodology

2.1. Flow Solution and Verification. The CFD solver used in this work is the open-source solver (named ADflow) [28, 29]. ADflow is a second-order finite-volume CFD solver that solves compressible flows and can handle structured multi-block and overset meshes [30]. ADflow has several turbulence models. In this paper, we use the Spalart-Allmaras (SA) model [31].

We validate the computation solver against experimental data of the low-speed airfoil E387 [32] at the Reynolds number of $Re = 3.5 \times 10^5$. In the experiment, a zigzag boundary layer trip was added on the top and bottom surfaces near the leading edge to ensure the flow was fully turbulent. We use the open-source pyhyp (https://github.com/mdolab/pyhyp) to generate a simulation mesh [33]. The cell number of the calculation mesh is 7.0×10^4, as shown in Figure 2. Figure 3 compares the simulation results and experimental data. Lift coefficients are well-matched in the linear region, although the lift curve slope of the simulation is slightly larger than the experimental data. The calculated drag polar curve (C_d is the drag coefficient) also shows an excellent agreement with the experimental data, especially in the region of the lift coefficient $C_l \in [0.4, 1.2]$, as shown in Figure 3(b). Simulation results indicate that ADflow is reliable and robust in low-speed airfoil aerodynamic analysis and can be used for optimization design research.

2.2. Adjoint-Based Optimization Approach. For aerodynamic optimizations of the tandem airfoil system, we use the MACH-Aero framework based on a discrete adjoint implementation [34–37], as shown in Figure 4. MACH framework embeds different modules, including ADflow (flow) solver, free form deformation (FFD) geometry parameterization, and volume mesh deformation (IDW mesh wrapping) module in the optimization loop. This framework provides an efficient, accurate gradient computation and gradient-based optimization [28].

In this work, the tandem airfoil system is parameterized using FFD volumes with pyGeo (https://github.com/mdolab/pygeo) [38, 39]. FFD control points move in the vertical direction to change airfoil shapes. Once airfoil shapes are deformed,
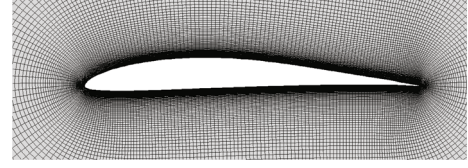

FIGURE 2: The calculation mesh of E387(e) airfoil.

the volume mesh used for the CFD solver is updated using IDwarp (https://github.com/mdolab/idwarp), which implements a mesh-warping algorithm [40, 41], with automatic differentiation in forward and reverse mode. Finally, in the MACH framework, the functions of interest and their gradients are provided to the gradient-based optimizer (https://github.com/mdolab/pyoptsparse) [42].

3. Data Mining Based on SOM

In this paper, the data mining method based on SOM is used. SOMs are neural networks that use unsupervised learning to transform or map multidimensional data to a regular low-dimensional grid with topological ordering [27]. The characteristics of the SOM algorithm make it mostly used for nonlinear projection of input data in high dimensional space onto two-dimensional space, extracting knowledge implicit in data, such as attributes and features.

For a data set consisting by n-dimensional vectors, every neural in SOM networks is represented by a n-dimensional weight vector $\boldsymbol{w} = [w_1, \cdots, w_n]$, where n is equal to the dimension of the input vectors. Each neural connects to adjacent neurons by a neighborhood relation, which dictates the map's topology. The SOM is trained iteratively. In each training step, one vector x from the input data set is chosen randomly, and the distances between it and all the weight vectors of the SOM are computed using the distance measure. The neuron, whose weight vector is closest to the vector x, is called the best-matching unit (BMU), denoted by w_c.

$$\|\boldsymbol{x} - \boldsymbol{w}_c\| = \min_j \{ \| \boldsymbol{x} - \boldsymbol{w}_j \| \}, \qquad (1)$$

where $\|\cdot\|$ is the distance measure, typically Euclidean distance.

After finding the BMU, the weight vectors of the SOM are updated so that the BMU and its neighborhood move closer to the input vector x in the input space. The weight vectors update rule is

$$\boldsymbol{w}_i(k + 1) = \boldsymbol{w}_i(k) + \alpha(k) h_{ci}(k)[\boldsymbol{x}(k) - \boldsymbol{w}_i(k)], \qquad (2)$$

where k denotes time, α is the learning rate, and $h_{ci}(k)$ is the neighborhood kernel around BMU. The neighborhood kernel is a nonincreasing function of time and neural distance from the BMU, which defines the region of influence that the input vector has on the SOM. The procedure of updating weight vectors stretches the BMU and its topological neighbors towards the input data set. Finally, the neurons on the grid become ordered, indicating that the neighboring neurons have similar weight vectors.
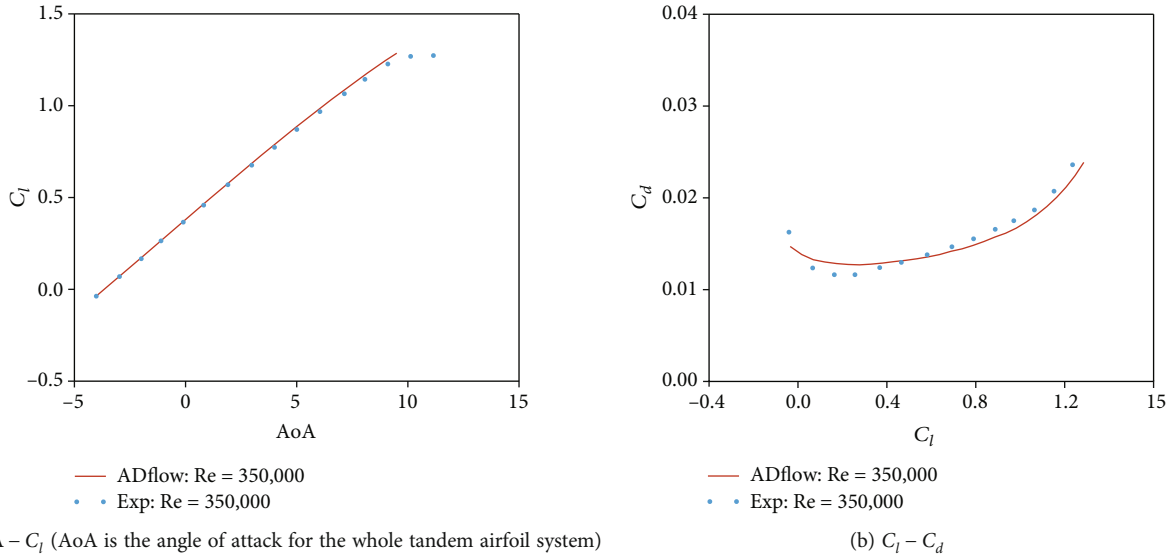
(a) AoA − C_l (AoA is the angle of attack for the whole tandem airfoil system)

(b) C_l − C_d

FIGURE 3: Aerodynamic calculation results for the E387 airfoil with experimental data of low speed at Re = 3.5×10^5.

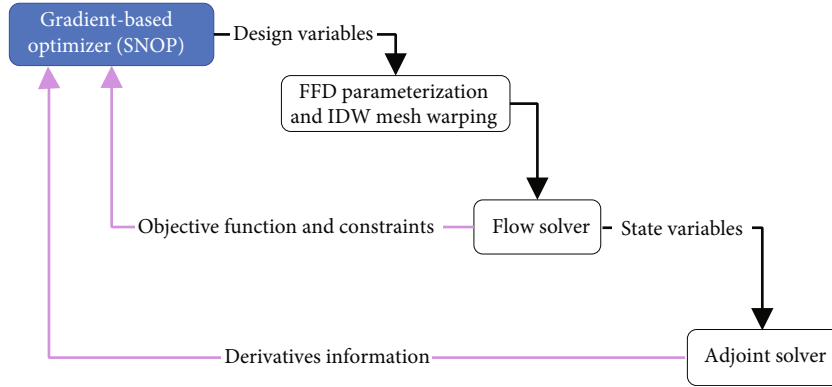
FIGURE 4: The framework of the adjoint-based aerodynamic optimization method.

In this paper, we use the free software SOM Toolbox$^{\parallel}$, which is an implementation of SOM and its visualization. In the SOM Toolbox, the topology of SOM can be shown in two ways: local lattice structure and global map shape. Among all local lattice structures, the hexagonal lattice structure is one of the most commonly used, as shown in Figure 5. This figure is the visualization of weights that connect each input to each neuron. Similar connection patterns of inputs illustrate the high correlation among these inputs. In the global map, the neurons are represented by points, and the adjacent neurons are connected by straight lines. During the SOM training process, the global map is continuously stretched to match the space of the input data set, as shown in Figure 6. The neurons with close color have similar weight vectors. In the global map, all points are colored into several different groups. Each group represents one neuron cluster obtained by SOM.

4. Design Space Exploration Using Data Mining

In this section, we utilize data mining in combination with an optimization method to explore the entire design space,

with the relative position serving as the variable parameter. Firstly, we conduct a mesh convergence study using the overset mesh. Next, we generate a sample with a capacity of six hundred and discuss the characteristics and correlations within the design space. It is important to note that the shape of the airfoil remains constant during this stage. Using the research conclusions on the design space characteristics, we select two representative sets of relative position parameters and optimize the airfoil shape using the adjoint-based optimization method. With the optimized airfoil, we again use SOM-based data mining to uncover the design space characteristics. We then compare our findings with different airfoils to examine the effects of airfoil shape on both the design space characteristics and aerodynamic performance.

4.1. Mesh Convergence Study. To ensure sufficient mesh resolution for the ADflow solver, we computed the aerodynamic forces of a tandem airfoil system using three overset mesh levels (L0, L1, and L2). Among all three meshes, the L0 mesh is the finest one. The first boundary layer cell height is set to 1×10^{-6} m, which makes the value of $y+$ below 1. This results in a total of 2.06×10^5 cells. Figure 7 shows the
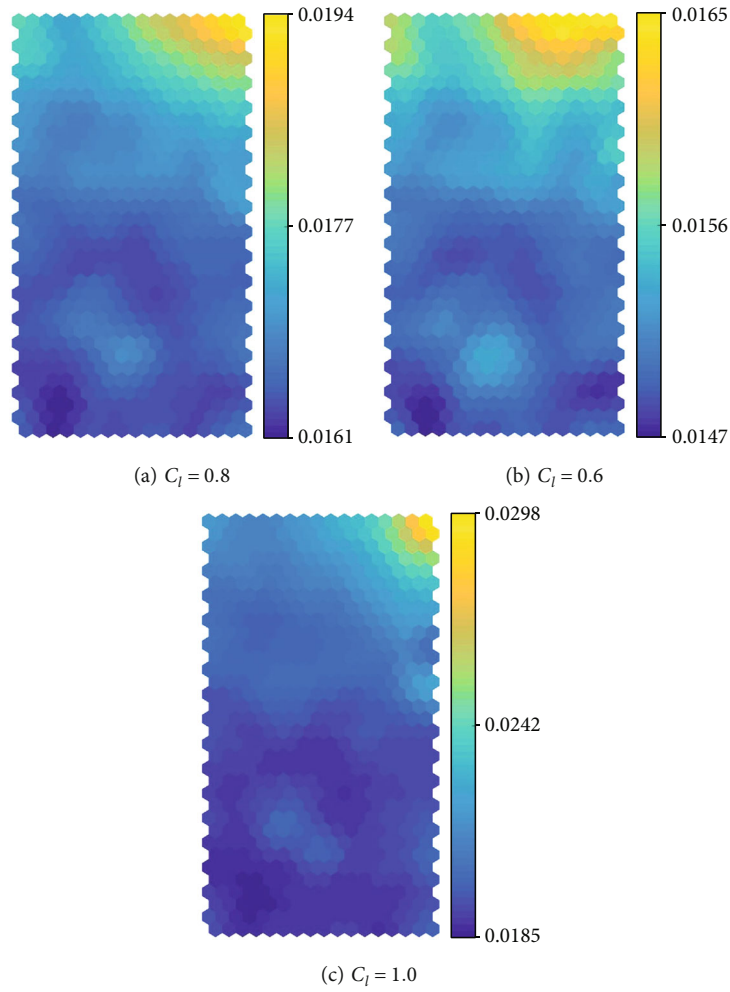
(a) $C_l = 0.8$

(b) $C_l = 0.6$

(c) $C_l = 1.0$

FIGURE 5: SOM map of C_d at three different C_l.

(a) Scatter plot C_{d1} vs. C_{d2}

(b) Scatter plot C_{d1} vs. C_{d3}

(c) SOM map C_{d1} vs. C_{d2}

(d) Scatter plot C_{d2} vs. C_{d3}

(e) SOM map C_{d1} vs. C_{d3}
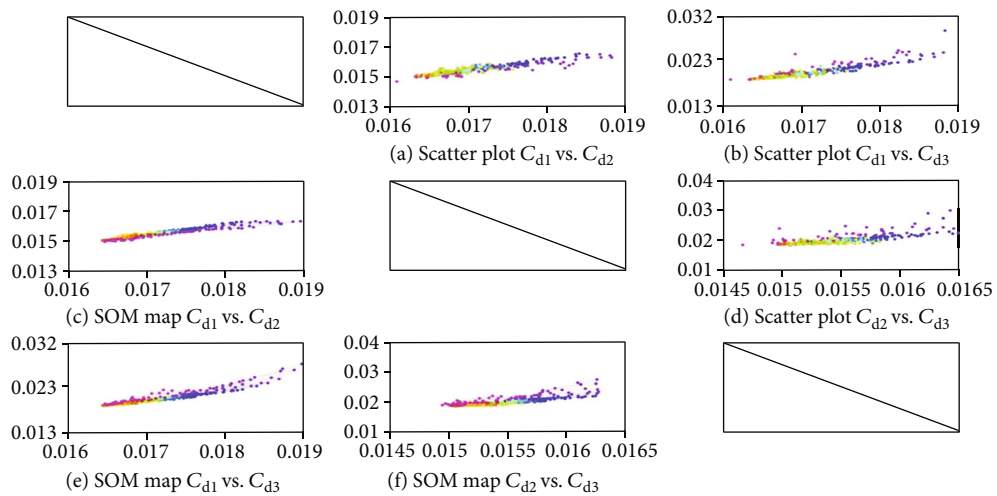
(f) SOM map C_{d2} vs. C_{d3}

FIGURE 6: The scatter plot and global SOM map of C_d at three different C_l.

topology of overset mesh and the grid distribution in the boundary layer. We coarsen L1 mesh from mesh L0 by removing every second cell in all three directions. Similarly, the mesh L2 is obtained by coarsening mesh L1.

Figure 8 shows the C_d of three-level meshes and the Richardson extrapolation value. The simulation condition is $V_\infty = 38m/s$ (free-stream velocity at infinity), $C_l = 0.8$, and $Re = 0.35 \times 10^6$. It is clear that the mesh L2 is very
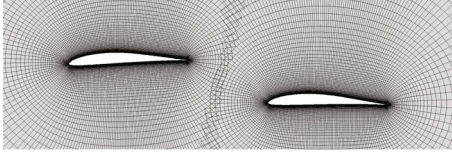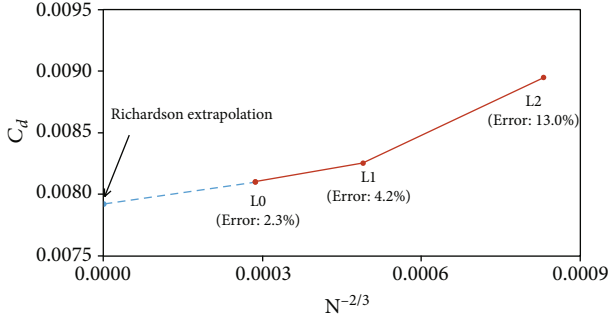
FIGURE 7: The overset mesh of a tandem airfoil system.

FIGURE 8: Richardson extrapolation about C_d at $C_l = \mathbf{0.8}$ and V_∞ = $\mathbf{38}$m/s for the grid convergence.

TABLE 1: Sample space range definition.

Range	Stagger	Gap	Decalage (°)	θ_1 (°)	θ_2 (°)
Lower limit	0.0	-3.0	-6	-3	-3
Upper limit	6.0	2.0	6	3	3

TABLE 2: Simulation conditions for sample generation.

Parameters	V_∞ (m/s)	Re (×10^6)	C_{l1}	C_{l2}	C_{l3}
Value	38	0.35	0.8	0.6	1.0

(0.6, 0.8, and 1.0) (The C_l target is reached by changing the angle of attack while keeping decalage constant.) of low-speed HALE UAVs. The cruise velocity is 38 m/s. We simulate the aerodynamic performance of tandem airfoil systems and extract the aerodynamic force coefficients of both the front and rear airfoils.

The uniform Latin hypercube method [44] is used to generate a sample with a capacity of six hundred. Among these sample points, the simulation of 8 sample points failed because of the geometrical position overlap of the two airfoils. Those invalid points are removed from the sample. For the optimization problem with four parameters, the valid sample capacity of 592 is large enough to cover the whole defined design space.

4.2.2. Correlation among Drag Coefficients at Different Lift Coefficients. Figure 5 shows the neuron clusters and color trends obtained by the SOM. The drag coefficients of the whole tandem airfoils system at three different lift coefficients show similar neuron clusters and color trends. Although the lift coefficients are different, drag coefficients have positive correlations. The region with low drag coefficients is located at the right-bottom of the maps.

Figure 6 shows scatter plots and global SOM maps, including all pairwise plots of total drag coefficients in a matrix format. The upper-right part of the matrix is the scatter plot, and the lower-left part is the global SOM map. In the figure, C_{d1}, C_{d2}, and C_{d3} correspond to the conditions of $C_l = 0.8$, $C_l = 0.6$, and $C_l = 1.0$, respectively. The result indicates a strong positive correlation among the total drag coefficients at the three selected C_l. Thus, the drag coefficients at three different lift coefficients are not in an obvious trade-off relation. The correlation clearly shows linear, especially in the low drag region.

4.2.3. Correlation between Relative Positions and Drag Coefficients. Correlations among drag coefficients at different lift coefficients indicate that from the perspective of exploring the low drag design space, the design space characteristics of any of the three simulation conditions can reflect the overall design trend in the given lift coefficients range. In this section, we investigate the design space characteristics of drag coefficients at $C_l = 0.8$ to discuss the correlation between relative position parameters and drag coefficients.

Figure 9 shows scatter plots and global SOM maps at $C_l = 0.8$. This figure shows the correlation between drag coefficients and relative position parameters, as well as the

coarse and yields a very different result. The C_d of mesh L0 and L1 is very close to the Richardson extrapolation value [43]. The relative error of mesh L0 and L1 relative to the Richardson extrapolation value is 2.3% and 4.2%, respectively, which are acceptable for design optimization research. In this work, we select the finest mesh L0.

4.2. Design Space Characteristics with Relative Positions as Design Parameters

4.2.1. Sample Generation. For tandem airfoils, relative position parameters directly affecting the aerodynamic performance are stagger, gap, and decalage. Those three parameters are defined in Figure 1. The stagger S describes the horizontal separation of the two airfoils, which is measured between the leading edges of the airfoils, and its value is always positive. The gap G defines the vertical distance between airfoils, which is also measured between the leading edges of the airfoils. The gap is positive when the front airfoil is above the rear airfoil. Both the stagger and gap are dimensionless by the chord of the airfoil. In this paper, the chord of both airfoils is equal. Decalage D is the relative angle between the two airfoils, and the value is positive when the front airfoil is at a higher angle of incidence. The θ_1 and θ_2 are the incidence angle of the front airfoil and rear airfoil, respectively, as shown in Figure 1, all of which rotate around the corresponding leading edge.

To generate a sample with ADflow, we change the front airfoil position in longitudinal and horizontal directions with the rear airfoil position fixed. As for the decalage, we change the angle of incidence of the two airfoils separately to vary the decalage. Table 1 shows the parameter space and the corresponding variation range of relative position parameters.

The simulation conditions and different lift coefficients are listed in Table 2. We choose three typical lift coefficients
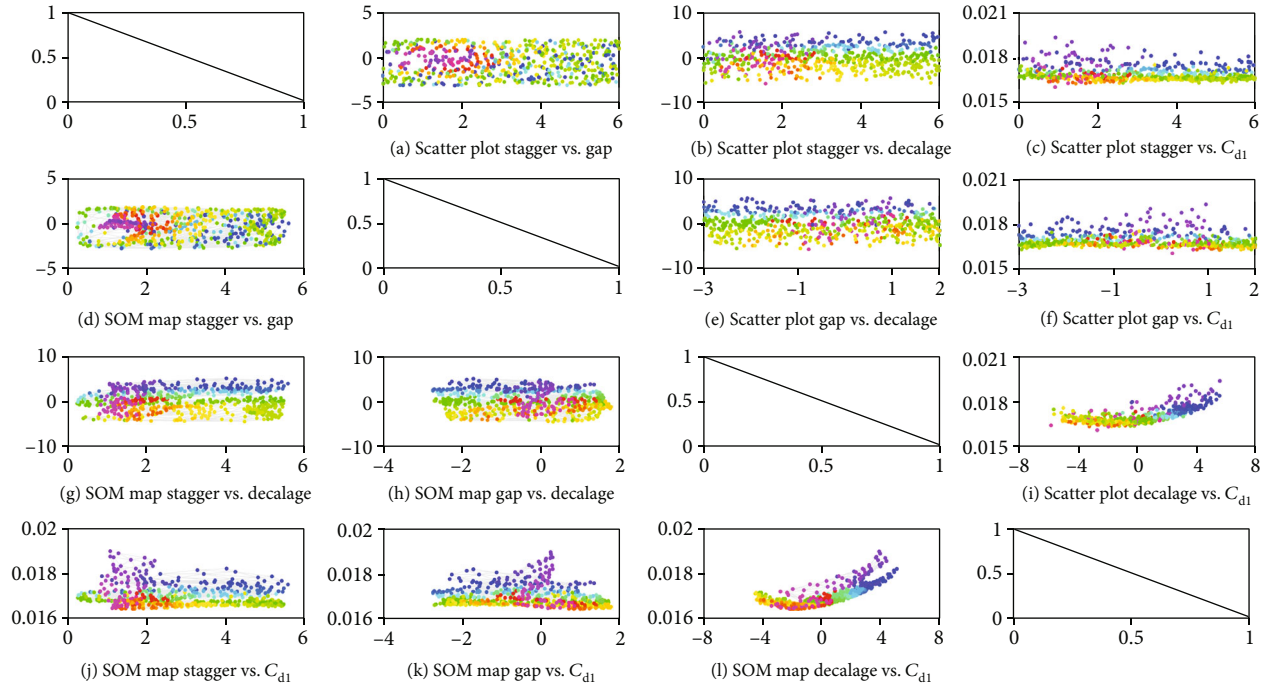
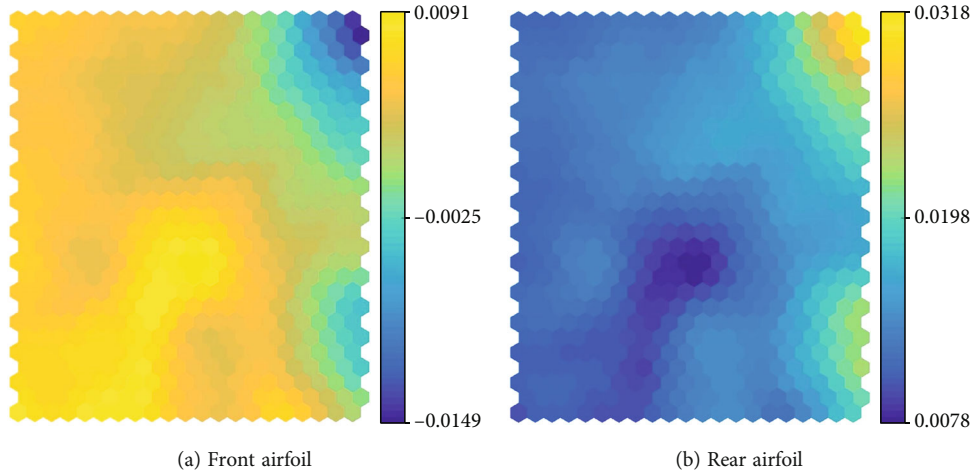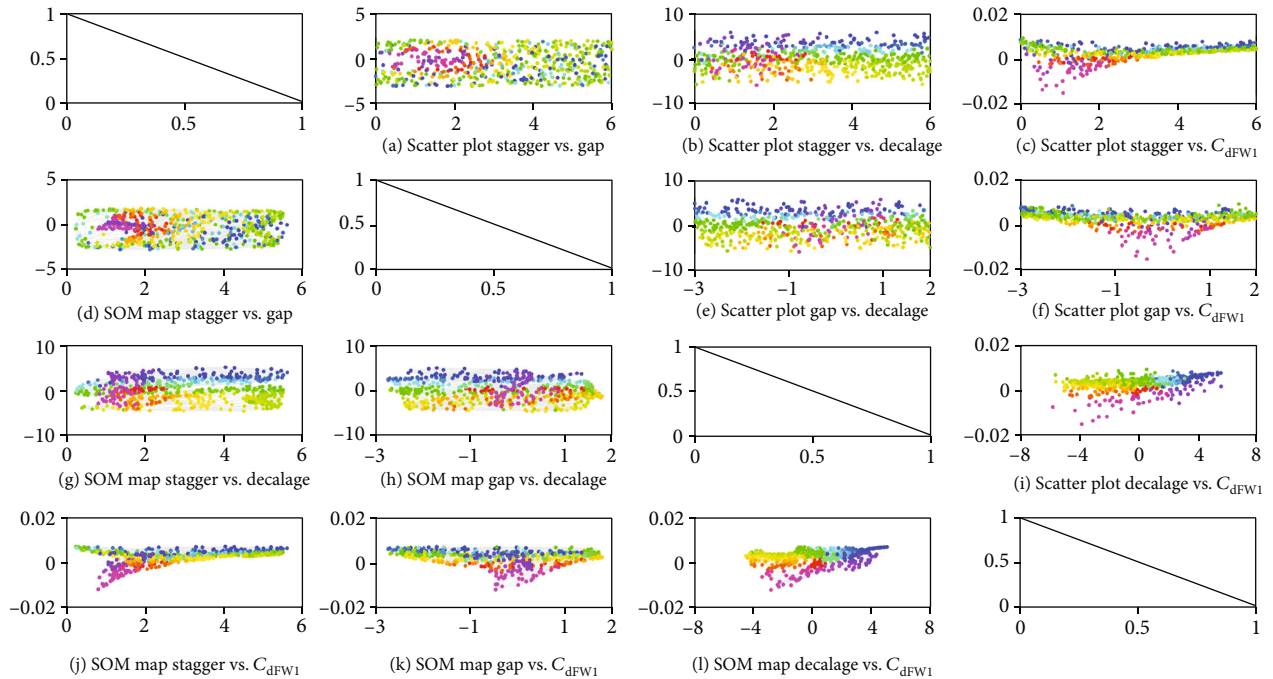FIGURE 9: The scatter plot and global SOM map of relative position parameters and C_d at $C_l = 0.8$.

relative position parameters. Besides, the SOM method divided all points into several clusters and colored different colors, which helps to understand the distribution of sample points in the design space. The result in Figure 9 shows that the low drag configuration concentrates in the region with negative decalage (shown in Figures 9(i) and 9(l)). Compared to decalage, the effect of the other two parameters (stagger and gap) on the total drag coefficient seems not apparent (shown in Figures 9(c) and 9(f)). The decalage and the total drag coefficient maintain a significant quadratic nonlinear relationship, as shown by the scatter plot and global SOM map in Figures 9(i) and 9(l). No matter what the values of stagger and gap are, the configuration with the lowest drag coefficients locates in the range of decalage around -2.5° (Figures 9(i) and 9(l)). With negative decalages, a small stagger, and a positive gap benefit to reduce the drag of the whole tandem airfoil system, as shown in Figures 9(c) and 9(f). The configuration with the lowest drag coefficient at $C_l = 0.8$ in the sample is a stagger of 0.924, a gap of 0.238, and a decalage of -2.69°.

4.2.4. Correlation between Relative Positions and Drag Coefficients of Each Airfoil of Tandem Airfoils. In this section, we study the relationship between relative positions and drag coefficients of each part of the tandem airfoils system to explore the design space characteristics and reveal the effect of flow interactions in-depth. Like the previous section, the research is based on the aerodynamic performance at $C_l = 0.8$.

Interestingly, the drag coefficient of the front airfoil and rear airfoil has similar neuron clusters and negative color trends, as shown in Figure 10. Figure 11 shows the scatter

plot and global SOM map of relative parameters and the front drag coefficient (C_{dFW1}) at $C_l = 0.8$. Figure 12 illustrates the scatter and global SOM plot of aerodynamic performance, including that of the front airfoil (C_{lFW1} and C_{dFW1}) and rear airfoil (C_{lRW1} and C_{dRW1}) at $C_l = 0.8$. The phenomenon shown in Figure 10 illustrates that based on the same airfoil, reducing the drag of one airfoil by changing relative position parameters causes the drag increase of the other airfoil simultaneously. The corresponding scatter plots and global SOM maps in Figures 12(e) and 12(h) clearly illustrate the strong approximate negative linear correlation between the drag of the front and rear airfoils. The rear airfoil drag coefficient is always positive. However, due to aerodynamic interference, the front airfoil drag coefficient is negative in a specific relative position parameter range (Figure 12(a)), which is the result of the circulation effect from the rear airfoil. This phenomenon is similar to the multielement airfoils, as described in the reference [9], and the details will be described in the next subsection.

The scatter plot and global SOM map of front airfoil drag coefficients C_{dFW} and parameter stagger S in Figures 11(c) and 11(j) show a bifurcation pattern in the sample space. As the stagger decreases from 6 to about 2, the drag coefficient of the front airfoil reduces in an approximately linear law. However, as the stagger further decreases, the variation of the front airfoil drag coefficients shows a strong nonlinearity with respect to the stagger. The scatter plot and global SOM map appear bifurcation, forming two branches with opposite trends. As the stagger decreases, the total variation trend of the front airfoil drag coefficient on the upper branch is drag increment, but on the lower branch, the trend is drag reduction. All sample points with

(a) Front airfoil   (b) Rear airfoil

FIGURE 10: SOM map of C_d of front and rear airfoils at $C_l = 0.8$.

(a) Scatter plot stagger vs. gap

(b) Scatter plot stagger vs. decalage

(c) Scatter plot stagger vs. C_{dFW1}

(d) SOM map stagger vs. gap

(e) Scatter plot gap vs. decalage

(f) Scatter plot gap vs. C_{dFW1}

(g) SOM map stagger vs. decalage

(h) SOM map gap vs. decalage

(i) Scatter plot decalage vs. C_{dFW1}

(j) SOM map stagger vs. C_{dFW1}

(k) SOM map gap vs. C_{dFW1}

(l) SOM map decalage vs. C_{dFW1}

FIGURE 11: The scatter plot and global SOM map of relative position parameters and C_{dFW1} at $C_l = 0.8$.

negative C_{dFW} are on the lower branch. Because of the approximate linear negative correlation between the drag of the front and rear airfoil, the scatter plot and global SOM map of the rear airfoil drag coefficient and parameter stagger would show a similar bifurcation pattern with opposite trends.

Aerodynamic interference mechanism changes are the reason for the appearance of the bifurcation pattern. When the value of the stagger is larger than 2.0, the aerodynamic interference between the front and rear airfoil is small because of a long horizontal distance. As a result, no matter what the value of the parameter gap is, the drag variation of each airfoil is limited. However, when the stagger is lower than 2.0, the effect of the other two parameters is gradually

magnified, as shown in Figures 11(f), 11(i), 11(k), and 11(l) (the rose-red color).

Most sample points on the lower branch with negative C_{dFW1} concentrated on the region of parameter stagger S lower than 2.0 and parameter gap G near 0.0. These sample points are colored by rose red, as shown in Figures 11(c) and 11(j). This region has two main features. Firstly, the two airfoils are close in spatial position, which causes a strong aerodynamic interference. Due to close coupling, induced upwash airflow from the rear airfoil to the front airfoil is more prominent in such a region. As for the front airfoil, the existence of upwash airflow increases the pressure peak on the upper surface, which causes the lift coefficient to increase and the pressure drag to decrease. Secondly, the
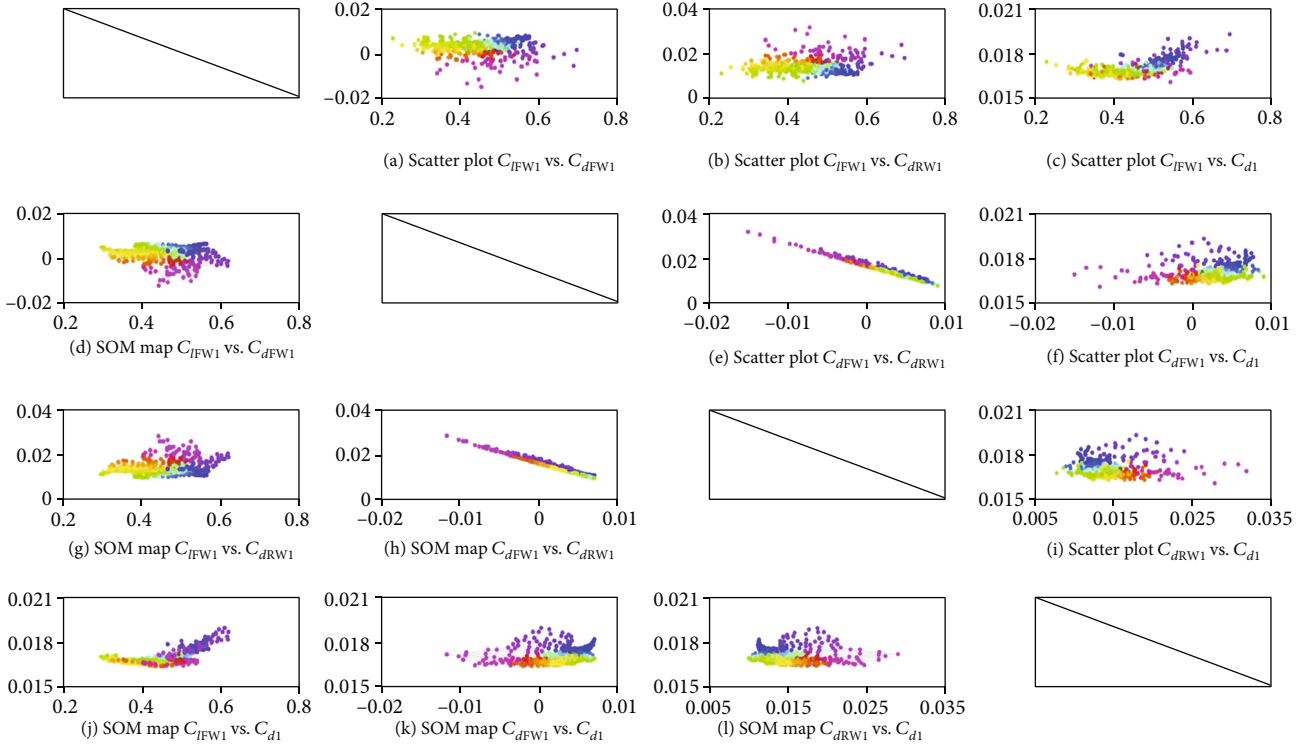
FIGURE 12: The scatter and global SOM plot of aerodynamic characteristics at $C_l = 0.8$.

two airfoils have almost the same angle of incidence, or the rear airfoil has a higher angle of incidence. This feature ensures that the lift increase of the front airfoil is mainly due to the favorable flow interference between the two airfoils. Thus, although the lift coefficient of the front airfoil is increased, the drag coefficient is still significantly reduced. Due to the negative linear correlation, the drag coefficient of the rear airfoil has an opposite variation law compared to the front airfoil.

The sample points with large drag coefficients C_{d1} are colored by dark purple and blue, as shown in Figures 12(c) and 12(j). In Figures 9(i) and 12(c), we can find that among these sample points, the lift coefficients of the front airfoil C_{lFW1} are significantly higher than that of the rear airfoil C_{lRW} (C_{lFW} is almost larger than 0.6), and the decalage is larger than 2.0° (Figure 9(i)). For the tandem airfoil, increasing the decalage and utilizing aerodynamic interference are two main ways to increase the lift coefficient of the front airfoil. With the definition of the decalage, a large decalage means that the angle of incidence of the front airfoil is much larger than that of the rear airfoil, which is one of the main factors increasing C_{lFW}. The increment in the lift coefficient caused by a large decalage leads to an increase in the drag coefficient C_{d1}. However, if the main reason causing the increment of C_{lFW} is aerodynamic interference between the front and rear airfoils, not a large decalage, the result is different. For the sample point with the lowest drag coefficient, the value of C_{lFW} is more than twice the value of C_{lRW} (Figure 12(c)). The value of decalage corresponding to the lowest drag coefficient is -2.69° (Figure 9(i)).
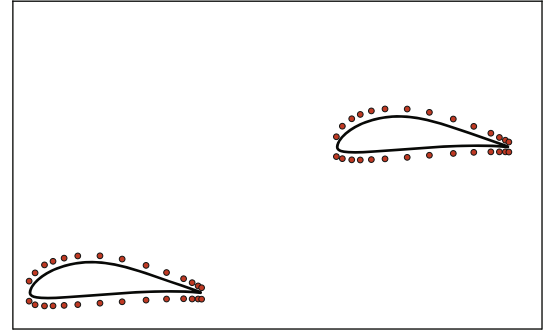

— Airfoil
• • FFD control points

FIGURE 13: FFD boxes for tandem airfoils.

TABLE 3: Tandem airfoil relative positions of the two aerodynamic shape optimization cases.

Cases	Stagger	Gap	Decalage (°)	θ_1 (°)	θ_2 (°)
Case1	0.924	0.238	-2.694	-1.726	0.968
Case2	5.174	1.259	-1.217	0.494	1.711

4.3. Aerodynamic Shape Optimization and Discussion. In this section, we introduce the airfoil shape optimization of the tandem airfoil with two sets of relative position parameters and discuss airfoil shape effects on design space characteristics and aerodynamic performance.
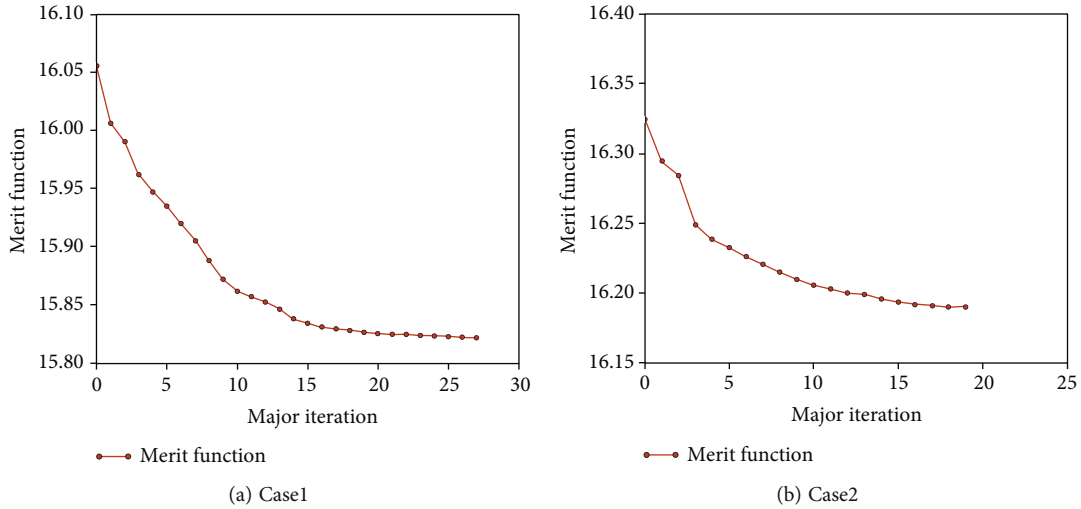
(a) Case1

(b) Case2

FIGURE 14: Convergence history for Case1 and Case2.

4.3.1. Design Optimization Problem. We select the configuration used in Section 4.2 as the initial geometry. The two FFD boxes are used to parameterize the tandem airfoil, as shown in Figure 13. Each FFD box has 14 control points chordwise and two control points in the normal direction. We fix the first and last row of control points chordwise to eliminate twist deformations caused by the movement of FFD control points. Thus, the optimization design problem has 48 geometrical design variables. These are control points that define the shape design variables (x). The thickness t constraints on both airfoils ensure enough volume and structure integrity. Besides, nose-down pitching moment (C_{My}) coefficients are considered. The optimization problem can be expressed as

$$\begin{aligned} &\text{minimize } C_d\\ &\text{With respect to } \quad \textbf{X}\\ &\text{subject to } \quad t \geq t_{\text{init}},\\ &\quad\quad |C_{My}| \leq C_{Myinit}, \end{aligned} \qquad (3)$$

where t_{init} is the initial thickness, and C_{Myinit} is the initial nose-down pitching moment (longitudinal moment).The main object of this paper is to research the tandem airfoil aerodynamic interferences with low drag coefficients, exploring design space characteristics. Exploring the effects of the airfoil shape on the aerodynamic drag coefficient and space characteristics is necessary. We selected two different sets of tandem airfoil relative positions to perform aerodynamic shape optimization. The shape optimization Case1 uses the relative positions of the tandem airfoil system with the lowest drag coefficient in Section 4.2. For Case1, the stagger is 0.924, showing that the front and rear airfoils have close-coupled interference. To consider the effect of far-coupled interference on shape design, we performed the shape optimization Case2 with a stagger around 5.174. The exact value of relative positions is determined by choosing parameters of the sample point with a low drag coefficient in the selected small region

of the sample. Table 3 shows the value of stagger, gap, and decalage of the two aerodynamic shape optimization cases.

Since drag coefficients among $C_l = 0.6$, 0.8, and 1.0 have strong positive correlations, for simplicity, a single-point optimization at $C_l = 0.8$ is used other than a multipoint design problem to explore the effect of airfoil shape on design space characteristics.

4.3.2. Optimization Results. Figure 14 illustrates the convergence history of both optimization cases. In this figure, the merit function is the combination of scaled objective function value C_d and constraint feasibility. More specifically, the merit function comprises the augmented Lagrangian, coupled with a quadratic penalty term for any constraint violations. Consequently, when all constraints are fulfilled towards the end of the optimization process, the merit function value becomes equivalent to the scaled objective value. Due to the small order of magnitude of the drag coefficient, the scaled coefficient of C_d component in the merit function is 10000. In detail, the merit function is defined as the augmented Lagrangian plus a quadratic penalty term for constraint violations and is used during line search to find an appropriate step length. When all constraints are satisfied towards the end of the optimization process, the merit function value is equal to the scaled objective function value (C_d).

Table 4 shows the improvement obtained by the optimization. Case1 and Case2 achieved about 1.8% and 1.28% drag reduction, respectively. In Table 4, C_{dp} is the pressure drag, and

C_{df} is the friction drag. The drag reduction mainly benefits from the decrease of pressure drag. From the aerodynamic force coefficients of each airfoil in a tandem airfoil system, we can study the change in aerodynamic characteristics more in-depth. After optimization, the drag of the front airfoil decreases, but the drag of the rear airfoil increases for Case1. However, the drag reduction of the front airfoil is larger than the drag increment of the rear airfoil.

TABLE 4: Comparisons of optimization results.

Case		Initial	Case1 optimized	Delta	Initial	Case2 optimized	Delta
	C_d	0.0161	0.0158	-1.80%	0.0164	0.0162	-1.28%
Tandem airfoil	C_{dp}	0.0049	0.0045	-7.82%	0.0052	0.0049	-6.30%
	C_{df}	0.0112	0.0114	0.98%	0.0112	0.0113	0.99%
	C_l	0.545	0.529	-2.86%	0.406	0.413	1.60%
Front airfoil	C_d	-0.0117	-0.0129	-10.26%	0.0039	0.0038	-2.56%
	C_{dp}	-0.0175	-0.0189	-7.71%	-0.0017	-0.0019	-9.88%
	C_{df}	0.0058	0.0059	2.24%	0.0056	0.0057	0.89%
	C_l	0.255	0.271	6.24%	0.394	0.388	-1.60%
Rear airfoil	C_d	0.0278	0.0287	3.24%	0.0125	0.0124	-0.80%
	C_{dp}	0.0224	0.0233	4.34%	0.0070	0.0068	-2.30%
	C_{df}	0.0054	0.0054	-0.37%	0.0055	0.0056	1.08%

(a) Airfoil shape comparison

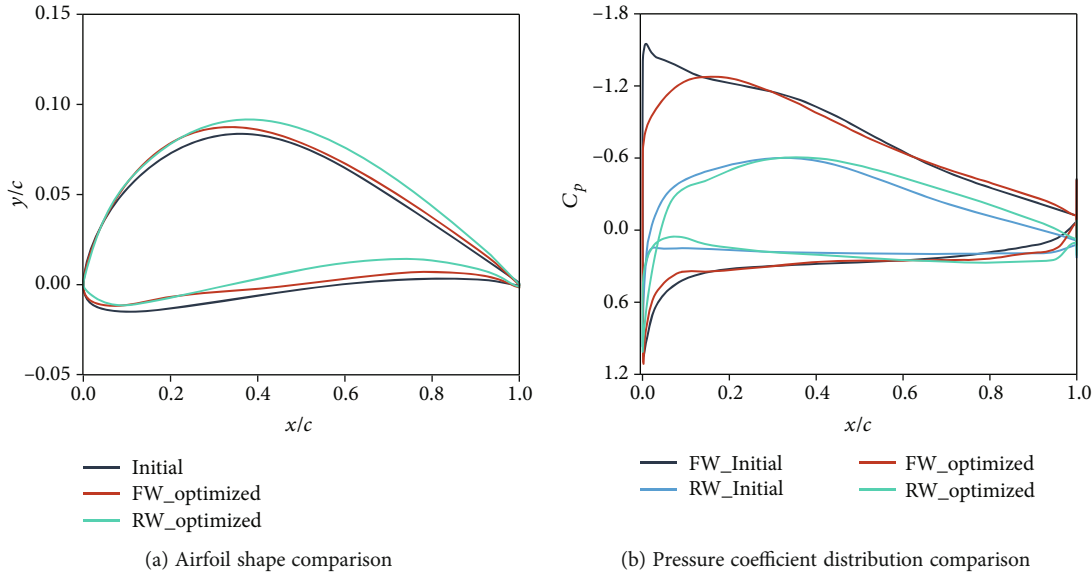(b) Pressure coefficient distribution comparison

FIGURE 15: Airfoils and pressure coefficient distribution optimization results of Case1. (FW: front airfoil; RW: rear airfoil.)

For Case2, the results are different, and the drag coefficients of the front and rear airfoil decrease.

From the comparison of airfoils in Case1 (shown in Figure 15), we can conclude that the camber increases and the leading edge radius decrease for the front and rear airfoils. The change in airfoils results in a decrease in the suction peaks of the pressure coefficient, and the pressure load at the rear part of the airfoils increases. The airfoil and pressure coefficient of Case2 has a similar but smaller change compared with Case1 (shown in Figure 16).

Figures 17 and 18 show C_p (pressure coefficient) contour plots of Case1 and Case2. For Case1, although the angle of attack of the front airfoil (-1.726°) is much smaller than that of the rear airfoil, the effective angle of attack is large.

This phenomenon is induced by the strong aerodynamic interference between the front and rear airfoil. The position of stagnation points can reflect it (Figure 17). For Case2, because of a relatively weak aerodynamic interference, the location of the stagnation point of the front and rear airfoil has no significant difference.

Figures 19 and 20 illustrate the pressure drag coefficient C_{dp}^e at each surface mesh cell of airfoils, which directly reflect the pressure drag contribution of each part. For Case1, the pressure drag coefficient C_{dp}^e on the lower surface of both front and rear optimized airfoils decreases to some extent. On the upper surface, because of the decrease in pressure peak, C_{dp}^e increases near the leading edge. Once leaving the leading edge area, C_{dp}^e decreases significantly. For the rear
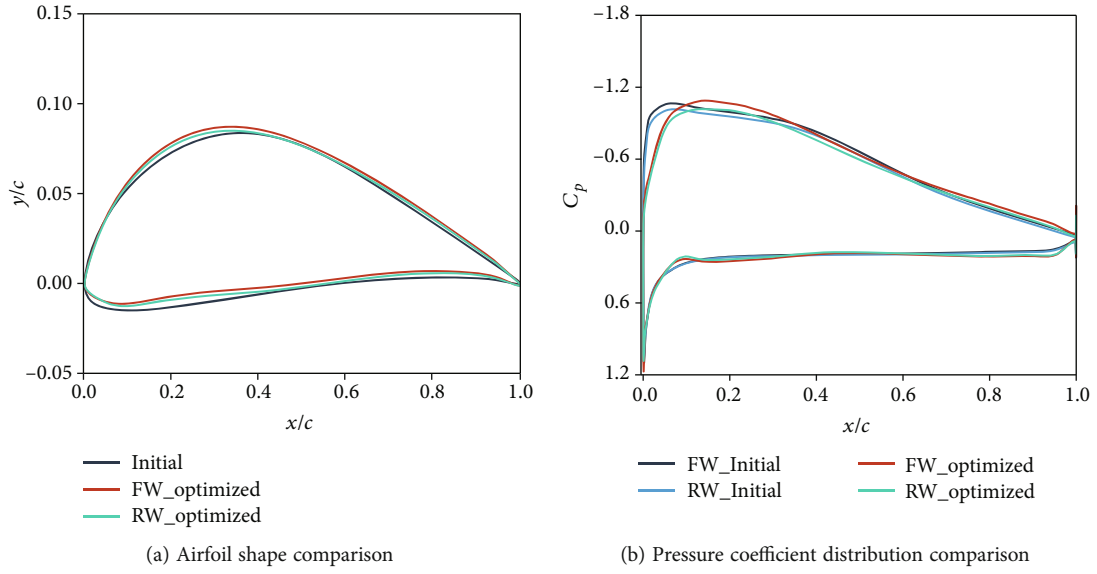
(a) Airfoil shape comparison

(b) Pressure coefficient distribution comparison

FIGURE 16: Airfoils and pressure coefficient distribution optimization results of Case2. (FW: front airfoil; RW: rear airfoil.)

(a) Initial

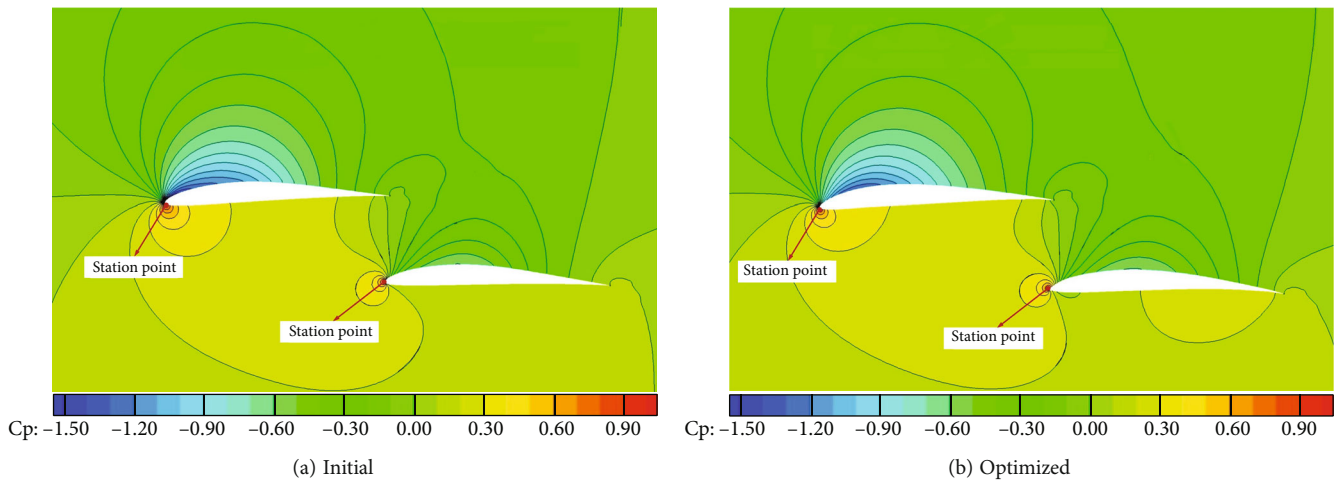(b) Optimized

FIGURE 17: C_p contour comparison of Case1.

(a) Initial

(b) Optimized
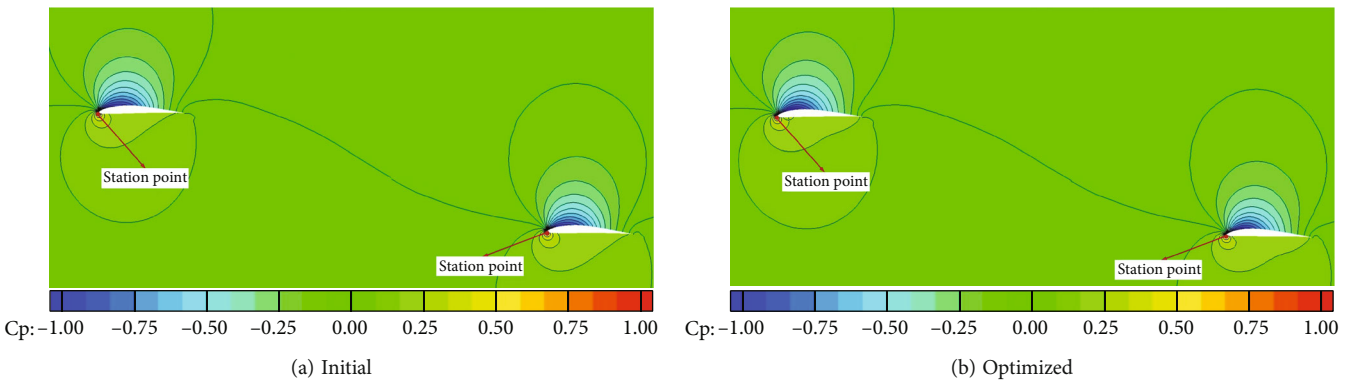
FIGURE 18: C_p contour comparison of Case2.

(a) Front airfoil comparison

(b) Rear airfoil comparison
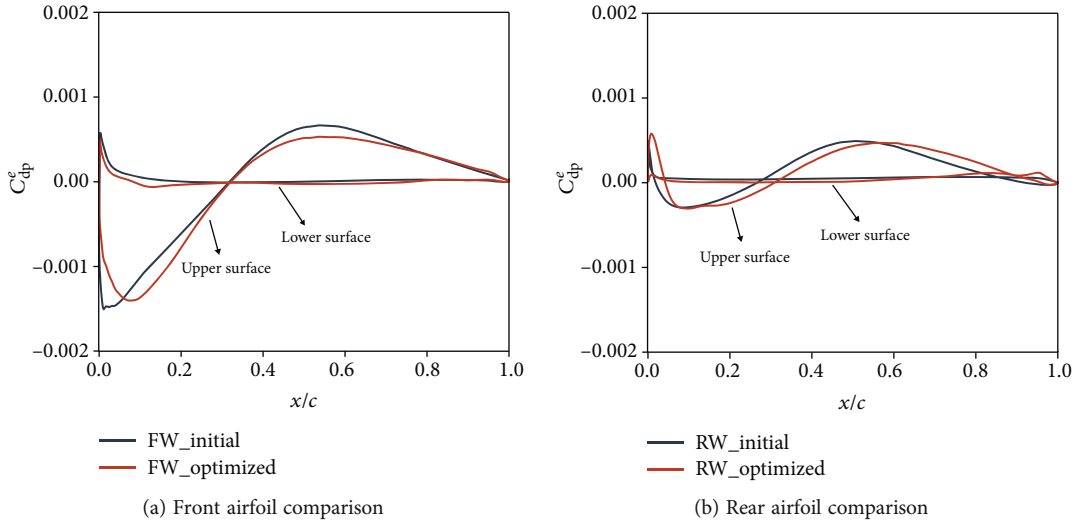
Figure 19: Comparisons for the C_{dp} distribution of Case1. (FW: front airfoil; RW: rear airfoil.)

(a) Front airfoil comparison

(b) Rear airfoil comparison
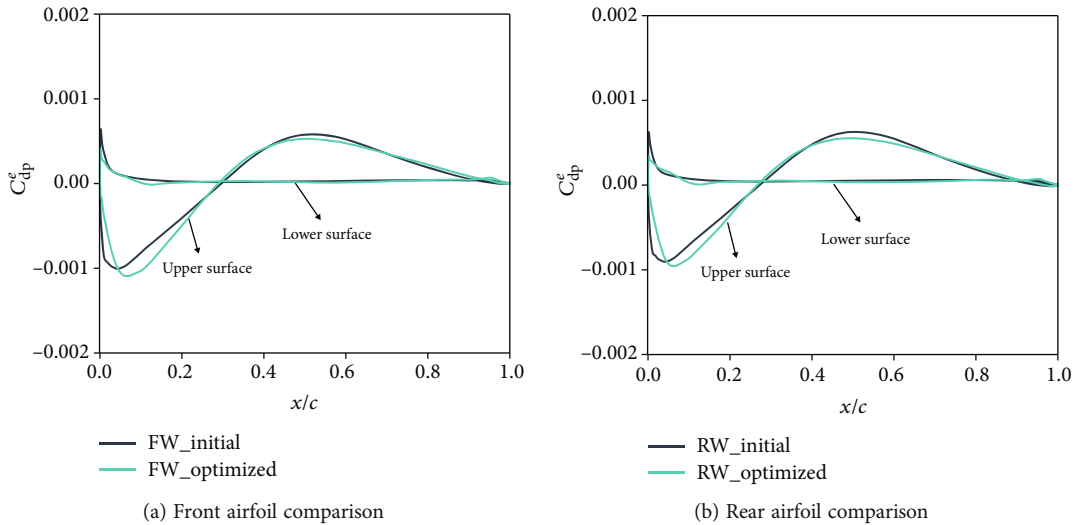
Figure 20: Comparisons for the C_{dp} distribution of Case2. (FW: front airfoil; RW: rear airfoil.)

airfoil, C_{dp}^e increases near the trailing edge. The C_{dp}^e variation of optimized airfoils of Case2 has a similar trend as the front airfoil of Case1, as shown in Figure 20.

4.3.3. Design Space Variation Analysis. Based on the same sample space generated in Section 4.2, we recalculate the aerodynamic performance of each sample point and obtain two updated sample sets. The updated two sample sets are from the optimized tandem airfoils of Case1 and Case2. We then use the SOM method to deal with the two sample sets to reveal the effects of the airfoil shape on aerodynamic performance and design space characteristics.

Figures 21 and 22 are the scatter and global SOM maps of Case1. Figure 21 shows the relationship among relative position parameters and the change of C_{d1} after optimization (represented by ΔC_{d1}). Figures 21(c), 21(f), and 21(i) clearly illustrate that the drag coefficient (C_{d1}) of most sample points is reduced (a negative value). Sample points col-

ored yellow and light brown corresponds to the points with the largest drag reduction. In contrast, the sample points colored blue and dark purple have the smallest drag reduction, and the C_{d1} of some sample points even increases significantly.Figures 21(a), 21(b), and 21(e) show the distribution of sample points in two-dimensional planes in the design space. In Figures 21(c), 21(f), and 21(i), we can find that the drag reduction value after optimization mainly depends on parameters decalage D. Sample points with positive decalage have more drag reduction than points with negative decalage. Among sample points with positive decalage, sample points distribute in the range of $S \in [0, 2.5]$ and $G \in [0, 2]$ (yellow and light brown color) have the largest drag reduction. The parameter space constructed by $S \in [0, 2.5]$ and $G \in [0, 2]$ has a similar aerodynamic close-coupled interference as the optimized result in Case1, which is the main reason that the sample points located in such parameter space have a large drag reduction.
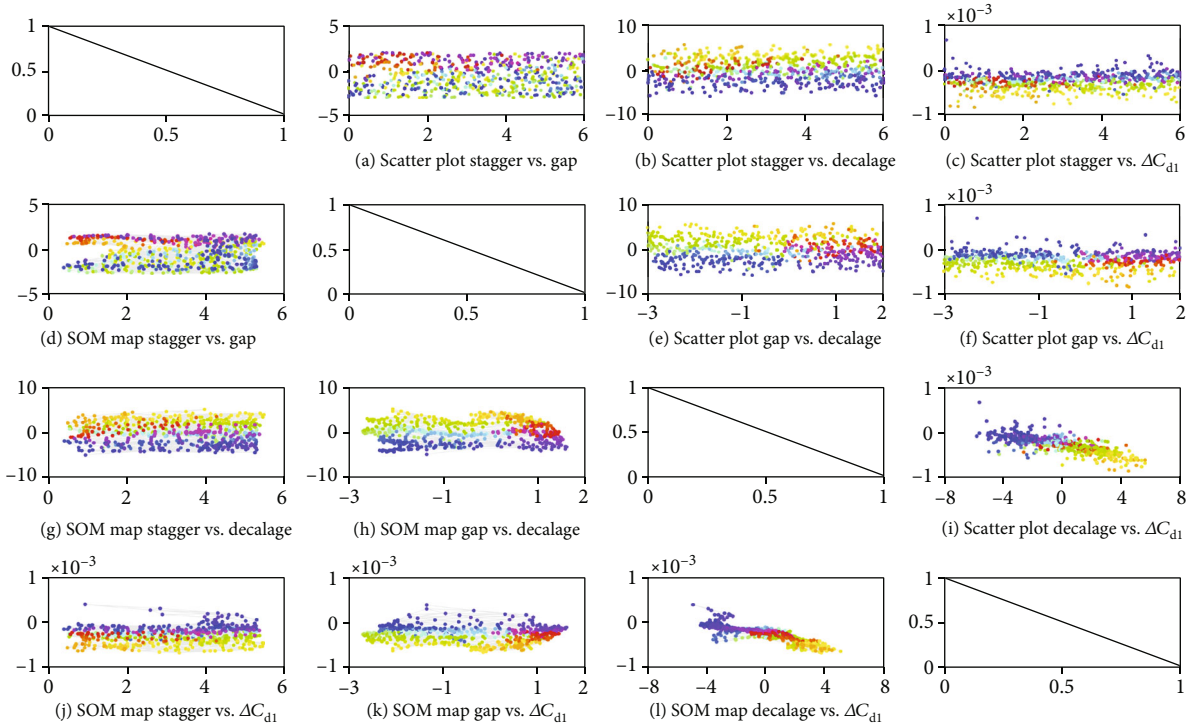
Figure 21: The scatter plot and global SOM map of relative position parameters and the changes of C_{d1} after optimization of Case1.
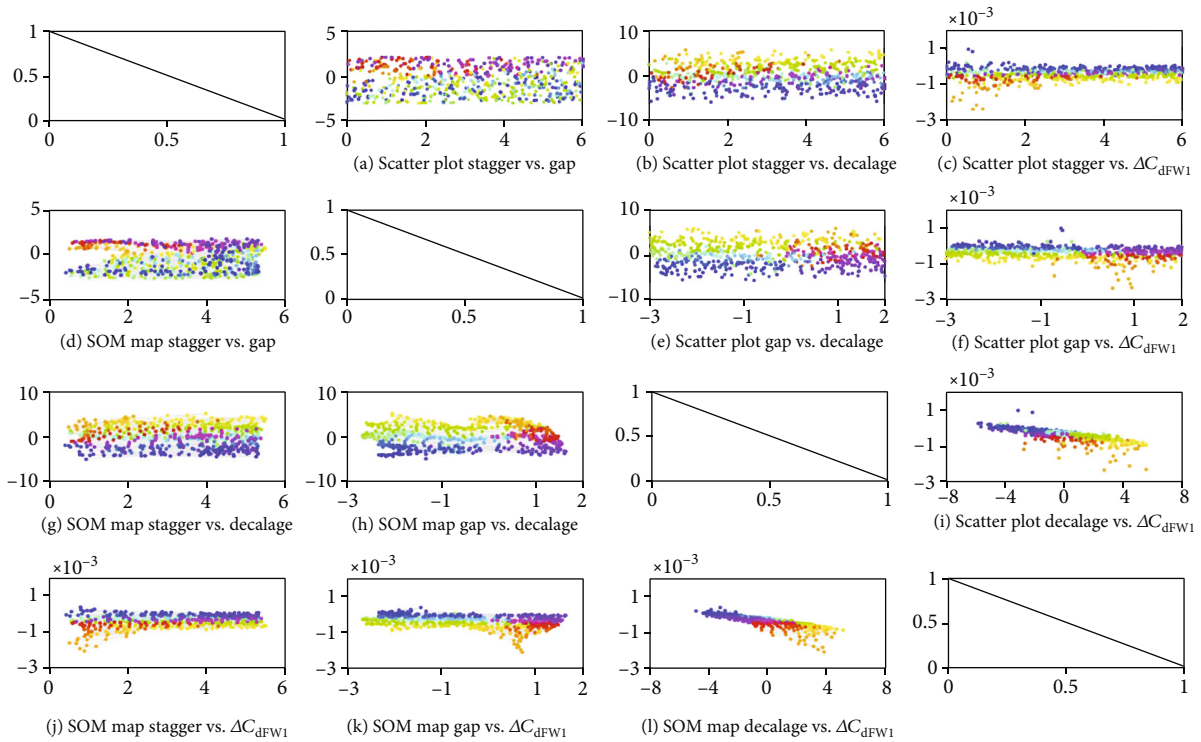

Figure 22: The scatter plot and global SOM map of relative position parameters and optimized C_{dFW1} of Case1.

Figure 22 shows the relationship among relative position parameters and the change of C_{dFW1} after optimization. The distribution of C_{dFW1} in the sample space is very similar with the distribution of C_{d1}.

Figures 23 and 24 are the scatter and global SOM maps based on optimal airfoils for Case2. Figure 23 illustrates the relationship among relative position parameters and the change of C_{d1} after optimization (represented by ΔC_{d1}). In
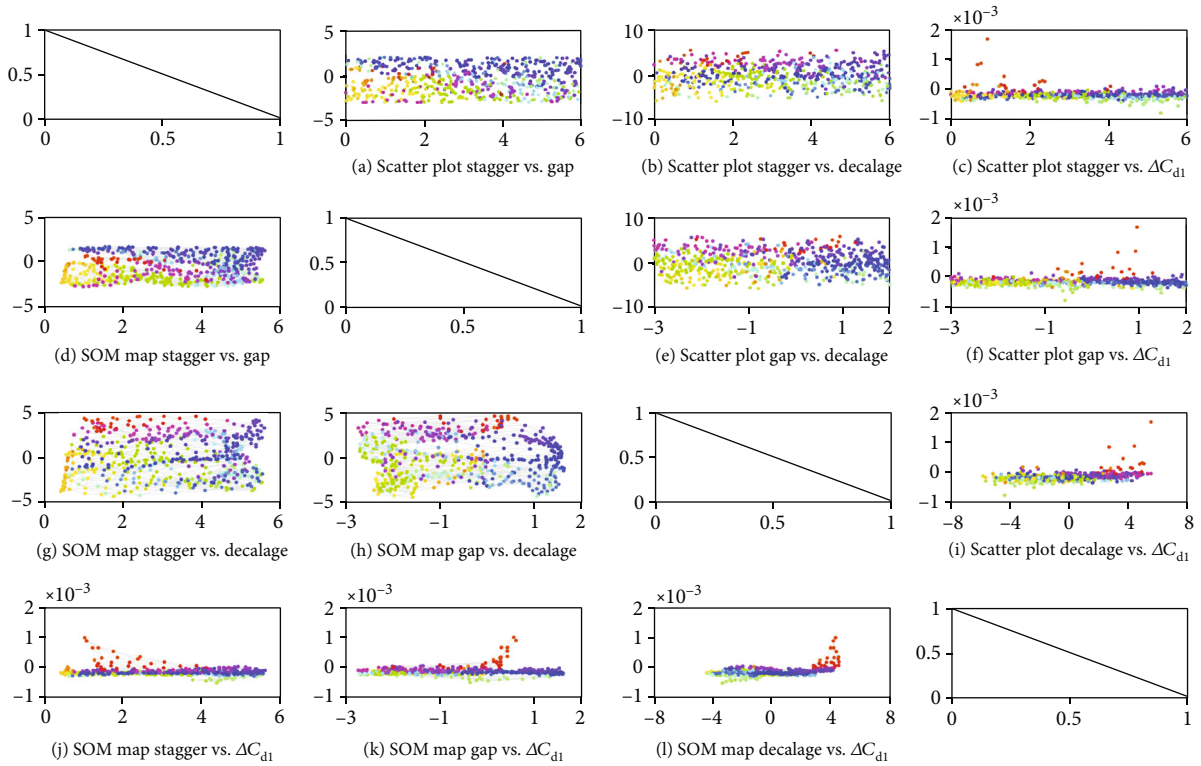
Figure 23: The scatter plot and global SOM map of relative position parameters and optimized C_{d1} of Case2.
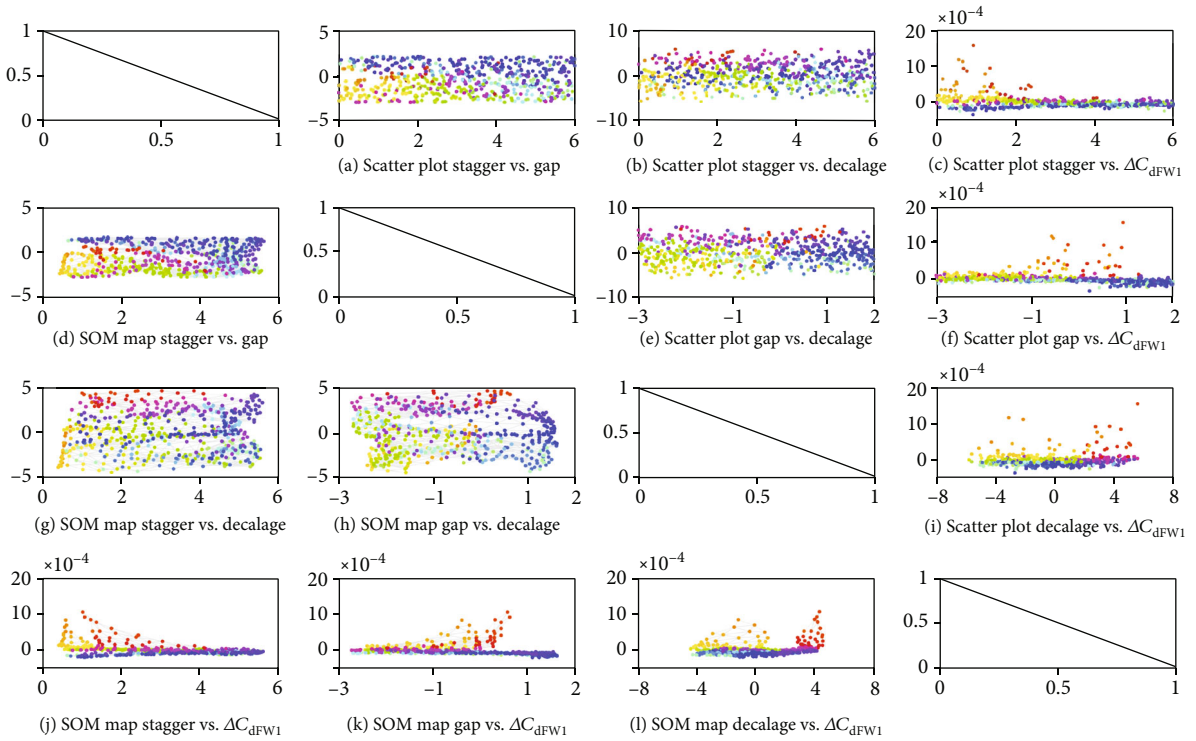

Figure 24: The scatter plot and global SOM map of relative position parameters and optimized C_{dFW1} of Case2.

Figures 23(c), 23(f), and 23(i), we can see that most sample points obtain drag reduction, which has the same trend as Case1. However, the distribution of drag reduction is not obvi-

ously dependent on the decalage D. In other words, the drag reduction range of sample points with different decalages does not vary much. This phenomenon is different from the

situation of Case1. Figures 23(c) and 23(f) also show the similar phenomenon. The main reason that causes such a phenomenon is the difference in aerodynamic interference strength between the front airfoil and the rear airfoil. For Case1, the tandem airfoil has a strong aerodynamic coupling interference. However, because of a larger stagger, the aerodynamic coupling interference of Case2 is weak. For Case2, the decrease of C_{d1} is mainly due to the reduction of airfoil profile drag. As a result, the airfoil, pressure distribution, and lift coefficient of both the front airfoil and rear airfoil are similar after optimization, as shown in Figure 16 and Table 4.

Figure 24 shows the relationship among relative position parameters and the change of $C_{d\text{FW1}}$ after optimization. We can see that the distribution of $\Delta C_{d\text{FW1}}$ in the sample space is similar to the distribution of ΔC_{d1}. The $\Delta C_{d\text{FW1}}$ is also independent on the decalage D. By comparing $\Delta C_{d\text{FW1}}$ of Case1 (Figure 22) and Case2 (Figure 24) in the whole sample space, it can be seen that most sample points of Case1 have a reduction in $C_{d\text{FW1}}$. However, there is a region where the $C_{d\text{FW1}}$ increases sharply for Case2. In Figures 24(c), 24(f), and 24(i), $C_{d\text{FW1}}$ of the sample points colored by brown and light brown increase significantly. These sample points concentrate in the region of $S \in [0, 2.5]$ and $G \in [-1.0, 1.0]$, where the aerodynamic interference between the front and rear airfoils is significant. The difference in aerodynamic coupling interference is the main reason that causes a significant increase of $C_{d\text{FW1}}$ in such a region.

5. Conclusions

This paper presents the adjoint-based aerodynamic optimization and data mining-based analysis for the tandem airfoil. The design space influenced by relative parameters and drag reduction mechanisms of the tandem airfoil system is explored.

Date mining technology based on the SOM method has been used to explore the design space and reveal the correlation between relative position parameters and aerodynamic force coefficients of the tandem airfoil systems. Results show that the drag coefficients at three selected lift coefficients have obvious positive linear correlations. The drag coefficient of the front airfoil $C_{d\text{FW}}$ and the rear airfoil $C_{d\text{RW}}$ has a strong linear negative correlation. In the design space constructed by relative position parameters, the drag of the whole tandem airfoil system significantly depends on the decalage D in an approximate quadratic relationship. Tandem airfoils with negative decalage around -2.5° have the smallest drag coefficient.

Different from the total drag C_d, the stagger S and gap G have an important impact on the drag coefficients of both the front airfoil ($C_{d\text{FW}}$) and the rear airfoil ($C_{d\text{RW}}$). As front and rear airfoils approach gradually, $C_{d\text{FW}}$ and $C_{d\text{RW}}$ change from an approximate linear variation to a nonlinear variation. In the range of $S \in [0, 2.5]$ and $G \in [-1.0, 1.0]$, the distribution of $C_{d\text{FW}}$ and $C_{d\text{RW}}$ in design space splits into two branches with the opposite trend. The variation of aerodynamic interferences between the front and rear airfoils is the main reason causing such phenomena.

We then performed two aerodynamic shape optimizations to study the optimal airfoil shape under different aerodynamic interferences between the front and rear airfoils. About 1.8% and 1.28% total drag reduction were obtained for Case1 and Case2, respectively. Because of a relatively strong aerodynamic interference of Case1, the camber of the optimized rear airfoil increased is larger than that of the front airfoil. For Case2, the large stagger determines that the aerodynamic interference is weak. As a result, the airfoil shapes and pressure distributions of the front airfoil and rear airfoil were very close.

Finally, we apply the data mining techniques to investigate the change of aerodynamic characteristics using the optimized aerodynamic shape in the design space constructed by relative position parameters. After the adoption of optimized airfoils of Case1, the region with large drag reduction in both C_d and $C_{d\text{FW}}$ locates in the range of $S \in [0, 2.5]$, $G \in [-1.0, 1.0]$, and $D \in [-6, 0]$. This region has strong aerodynamic interferences, similar to the optimization condition of Case1. In comparison, the drag reduction distribution in the whole design space is relatively more uniform with the optimized airfoils for Case2. This can be explained that most of the drag reduction of Case2 comes from the decrease of the airfoil profile drag. The summarized conclusion would guide the aerodynamic design of the joint-wing configuration. Furthermore, the established methods and the analysis approaches would be used to reveal the design space for aerodynamic design in the future.

Data Availability

All the available data are in the manuscript.

Ethical Approval

This article does not contain any studies with human participants or animals performed by any of the authors.

Consent

Informed consent was obtained from all individual participants included in the study.

Conflicts of Interest

On behalf of all authors, the corresponding author states that there is no conflict of interest.

Acknowledgments

References

[1] J. Wolkovitch, "The joined wing: an overview," *Journal of Aircraft*, vol. 23, no. 3, pp. 161–178, 1986.

[2] D. Lucia, "The sensorcraft configurations: a non-linear aero-servoelastic challenge for aviation," in *46th AIAA/ASME/ASCE/AHS/ASC Structures, Structural Dynamics and Materials Conference*, p. 1943, Austin, Texas, 2005.

[3] R. Cavallaro and L. Demasi, "Challenges, ideas, and innovations of joined-wing configurations: a concept from the past, an opportunity for the future," *Progress in Aerospace Sciences*, vol. 87, pp. 1–93, 2016.

[4] S. A. Andrews and R. E. Perez, "Comparison of box-wing and conventional aircraft mission performance using multidisciplinary analysis and optimization," *Aerospace Science and Technology*, vol. 79, pp. 336–351, 2018.

[5] E. Cestino, "Design of solar high altitude long endurance aircraft for multi payload & operations," *Aerospace Science and Technology*, vol. 10, no. 6, pp. 541–550, 2006.

[6] K. Wang, Z. Zhou, X. Zhu, and X. Xu, "Aerodynamic design of multi-propeller/wing integration at low Reynolds numbers," *Aerospace Science and Technology*, vol. 84, pp. 1–17, 2019.

[7] T. Phiboon, K. Khankwa, N. Petcharat et al., "Experiment and computation multi-fidelity multi-objective airfoil design optimization of fixed-wing UAV," *Journal of Mechanical Science and Technology*, vol. 35, no. 9, pp. 4065–4072, 2021.

[8] L. D. Palma, N. Paletta, and M. Pecora, "Aeroelastic design of a joined-wing UAV," in *SAE Technical Paper*, Pennsylvania, Harrisburg, US, 2009.

[9] A. M. O. Smith, "High-lift aerodynamics," *Journal of Aircraft*, vol. 12, no. 6, pp. 501–530, 1975.

[10] Z. Chen, X. Li, and L. Chen, "Enhanced performance of tandem plunging airfoils with an asymmetric pitching motion," *Physics of Fluids*, vol. 34, no. 1, article 011910, 2022.

[11] K. Rokhsaz, *Analytical Investigation of the Aerodynamic Characteristic of Dual Wing Systems, [Ph.D. Thesis]*, University of Missouri, 1980.

[12] M. D. Rhodes and B. Selberg, "Benefits of dual wings over single wings for high-performance business airplanes," *Journal of Aircraft*, vol. 21, no. 2, pp. 116–127, 1984.

[13] S. LeDoux, J. Vassberg, G. Fatta, and M. Dehaan, "Aerodynamic cruise design of a joined wing SensorCraft," in *26th AIAA Applied Aerodynamics Conference*, p. 7190, Honolulu, Hawaii, 2008.

[14] J.-M. Moschetta and C. Thipyopas, "Aerodynamic performance of a biplane micro air vehicle," *Journal of Aircraft*, vol. 44, no. 1, pp. 291–299, 2007.

[15] R. Jones, D. Cleaver, and I. Gursul, "Aerodynamics of biplane and tandem wings at low Reynolds numbers," *Experiments in Fluids*, vol. 56, no. 6, p. 124, 2015.

[16] X. Wen, Y. Liu, Z. Li, Y. Chen, and D. Peng, "Data mining of a clean signal from highly noisy data based on compressed data fusion: a fast-responding pressure-sensitive paint application," *Physics of Fluids*, vol. 30, no. 9, article 097103, 2018.

[17] C. Kong, J. Chang, Y. Li, and Z. Wang, "A deep learning approach for the velocity field prediction in a scramjet isolator," *Physics of Fluids*, vol. 33, no. 2, article 026103, 2021.

[18] A. A. Mishra, J. Mukhopadhaya, J. Alonso, and G. Iaccarino, "Design exploration and optimization under uncertainty," *Physics of Fluids*, vol. 32, no. 8, article 085106, 2020.

[19] Z. Li and X. Zheng, "Review of design optimization methods for turbomachinery aerodynamics," *Progress in Aerospace Sciences*, vol. 93, pp. 1–23, 2017.

[20] Y. Lian, A. Oyama, and M. S. Liou, "Progress in design optimization using evolutionary algorithms for aerodynamic problems," *Progress in Aerospace Sciences*, vol. 46, no. 5-6, pp. 199–223, 2010.

[21] X. Du, P. He, and J. R. Martins, "Rapid airfoil design optimization via neural networks-based parameterization and surrogate modeling," *Aerospace Science and Technology*, vol. 113, article 106701, 2021.

[22] K. Chiba and S. Obayashi, "Knowledge discovery for flyback-booster aerodynamic wing using data mining," *Journal of Spacecraft and Rockets*, vol. 45, no. 5, pp. 975–987, 2008.

[23] A. Oyama, T. Nonomura, and K. Fujii, "Data mining of Pareto-optimal transonic airfoil shapes using proper orthogonal decomposition," *Journal of Aircraft*, vol. 47, no. 5, pp. 1756–1762, 2010.

[24] Z. Guo, L. Song, Z. Zhou, J. Li, and Z. Feng, "Multi-objective aerodynamic optimization design and data mining of a high pressure ratio centrifugal impeller," *Journal of Engineering for Gas Turbines and Power*, vol. 137, no. 9, article 092602, 2015.

[25] A. Amrit, L. Leifsson, and S. Koziel, "Multi-fidelity aerodynamic design trade-off exploration using point-by-point Pareto set identification," *Aerospace Science and Technology*, vol. 79, pp. 399–412, 2018.

[26] P. Wu, P. Wang, and H. Gao, "Dynamic mode decomposition analysis of the common research model with adjoint-based gradient optimization," *Physics of Fluids*, vol. 33, no. 3, article 035123, 2021.

[27] T. Kohonen, "Exploration of very large databases by self-organizing maps," *Proceedings of International Conference on Neural Networks (ICNN'97)*, vol. 1, pp. PL1–PL6, 1997.

[28] G. K. Kenway, C. A. Mader, P. He, and J. R. Martins, "Effective adjoint approaches for computational fluid dynamics," *Progress in Aerospace Sciences*, vol. 110, article 100542, 2019.

[29] A. Yildirim, G. K. Kenway, C. A. Mader, and J. R. Martins, "A Jacobian-free approximate Newton-Krylov startup strategy for RANS simulations," *Journal of Computational Physics*, vol. 397, article 108741, 2019.

[30] N. R. Secco and J. R. Martins, "RANS-based aerodynamic shape optimization of a strut-braced wing with overset meshes," *Journal of Aircraft*, vol. 56, no. 1, pp. 217–227, 2019.

[31] P. Spalart and S. Allmaras, "A one-equation turbulence model for aerodynamic flows," in *30th aerospace sciences meeting and exhibit*, p. 439, Reno, NV, USA, 1992.

[32] M. S. Selig and B. D. McGranahan, "Wind tunnel aerodynamic tests of six airfoils for use on small wind turbines," *Journal of Solar Energy Engineering*, vol. 126, pp. 986–1001, 2004.

[33] N. R. Secco, J. P. Jasa, G. K. Kenway, and J. R. Martins, "Component-based geometry manipulation for aerodynamic shape optimization with overset meshes," *AIAA Journal*, vol. 56, no. 9, pp. 3667–3679, 2018.

[34] G. K. Kenway and J. R. Martins, "Aerodynamic shape optimization of the CRM configuration including buffet-onset conditions," in *54th AIAA Aerospace Sciences Meeting*, p. 1294, San Diego, California, USA, 2016.

[35] Z. Lyu and J. R. Martins, "Aerodynamic shape optimization of an adaptive morphing trailing-edge wing," *Journal of Aircraft*, vol. 52, no. 6, pp. 1951–1970, 2015.

[36] N. Bons, C. A. Mader, J. R. Martins, A. Cuco, and F. Odaguil, "High-fidelity aerodynamic shape optimization of a full configuration regional jet," in *2018 AIAA/ASCE/AHS/ASC Structures, Structural Dynamics, and Materials Conference*, p. 0106, Kissimmee, Florida, 2018.

[37] J. R. Martins and G. Kennedy, "Enabling large-scale multidisciplinary design optimization through adjoint sensitivity analysis," in *AIAA Scitech 2019 Forum*, p. 1702, San Diego, California, 2019.

[38] G. Kenway, G. Kennedy, and J. Martins, "A CAD-free approach to high-fidelity aerostructural optimization," in *13th AIAA/ISSMO multidisciplinary analysis optimization conference*, p. 9231, Fort Worth, Texas, 2010.

[39] Y. Yu, Z. Lyu, Z. Xu, and J. R. Martins, "On the influence of optimization algorithm and initial design on wing aerodynamic shape optimization," *Aerospace Science and Technology*, vol. 75, pp. 183–199, 2018.

[40] E. Luke, E. Collins, and E. Blades, "A fast mesh deformation method using explicit interpolation," *Journal of Computational Physics*, vol. 231, no. 2, pp. 586–601, 2012.

[41] G. K. Kenway and J. R. Martins, "Multipoint aerodynamic shape optimization investigations of the common research model wing," *AIAA Journal*, vol. 54, no. 1, pp. 113–128, 2016.

[42] R. E. Perez, P. W. Jansen, and J. R. Martins, "PyOpt: a python-based object-oriented framework for nonlinear constrained optimization," *Structural and Multidisciplinary Optimization*, vol. 45, no. 1, pp. 101–118, 2012.

[43] C. Brezinski and M. R. Zaglia, *Extrapolation Methods : Theory and Practice*, Elsevier, 2013.

[44] M. D. Shields and J. Zhang, "The generalization of Latin hypercube sampling," *Reliability Engineering & System Safety*, vol. 148, pp. 96–108, 2016.